SUPPLEMENTARY METHODS

Anatomical Preprocessing in *fMRIPrep*

First, each participant's T1-weighted (T1w) image was corrected for intensity non-uniformity using the N4 algorithm (Tustison et al., 2010). Each T1w image was then skull-stripped with a Nipype (Gorgolewski et al., 2011) implementation of the ANTs brain extraction workflow, using OASIS30ANTs as the target template. Brain-extracted T1w scans were subsequently registered to the brain-extracted 1-mm MNI152NLin6Asym template using SyN diffeomorphic registration (ANTs 2.2.0; Avants & Gee, 2004; Avants et al., 2008), and brain surfaces were reconstructed using FreeSurfer 6.0.1 (Dale et al., 1999; http://surfer.nmr.mgh.harvard.edu). Subject-level CSF, WM, and gray matter (GM) segmentations were performed on brain-extracted T1-weighted scans using FSL *fast* (FSL 5.0.9; Zhang et al., 2001).

Amyloid PET Analysis

Amyloid PET data were processed with in-house software. First, attenuation-corrected dynamic image frames were motion-corrected using *mcflirt* rigid-body registration (FSL 5.0.9; Jenkinson et al., 2002; Smith et al., 2004). The resulting motion-corrected PET frames were averaged and aligned with participants' T1-weighted structural MRI scans using ANTs rigid-body registration with a mutual information metric (Avants & Gee, 2004; Avants et al., 2008). Each anatomical MRI was segmented into cortical, subcortical, and cerebellar ROIs using a multi-atlas segmentation method (Asman & Landman, 2013; Wang et al., 2013). Mean tracer uptake in the cerebellar gray and white matter was computed and used as a reference to generate a standardized uptake value ratio (SUVR) map for the entire brain. A composite ROI consisting of the middle frontal, anterior cingulate, posterior cingulate, inferior parietal, precuneus, supramarginal, middle temporal, and superior temporal cortical regions was used to compute a global SUVR for amyloid scans (Landau et al., 2013).

ROI-based Representation of the Extended MTL Network

Extra-MTL ROIs with positive functional connectivity (FC) to the MTL were selected from the 400-region 17-Network Schaefer et al. (2018) parcellation. Cortical regions with connectivity to the MTL were identified in normal agers only [i.e., CU young, middle-aged, and Aβ− older participants]. To test for the presence of FC to the MTL, we performed 4 sets (one per each MTL ROI: left anterior, right anterior, left posterior, right posterior) of one-sample positive-sided *t*-tests [FDR-corrected, $q < 0.05$] on Fisher-transformed subject-level Pearson correlation coefficients, representing that segment's FC to each of the 393 non-MTL Schaeffer ROIs. Seven Schaeffer ROIs were excluded because of substantial (>15%) spatial overlap with our anterior or posterior tau-based MTL seeds. To ensure that we did not miss any major cortical regions with FC to the MTL, we also performed seed-to-voxel network identification. Here, one-sample permutation tests (5,000 permutations) for positive connectivity to the bilateral anterior and posterior tau-based MTL ROIs were performed on Fisher-transformed subject-level voxelwise seed-to-voxel connectivity maps (Conn 20.b; Whitfield-Gabrieli & Nieto-Castanon, 2012). The Threshold-Free Cluster Enhancement (TFCE) method with the FDR ($q < .05$) correction for multiple hypothesis testing was used in these voxelwise tests (Benjamini & Hochberg, 1995; Smith & Nichols, 2009). We considered a given Schaeffer ROI as a part of the broader MTL-associated functional system if it was functionally connected to at least one of the MTL ROIs in the ROI-to-ROI network identification or if more than 40% of that ROI's voxels corresponded to a statistically significant cluster in the voxelwise network identification method. In total, we identified 221 Schaeffer ROIs with positive functional connectivity to the MTL. Together with 4 seed regions, these 221 Schaeffer ROIs (225 ROIs in total) were used in all subsequent analyses of the MTL network function (Fig. 2a in the main text).

SUPPLEMENTARY FIGURES

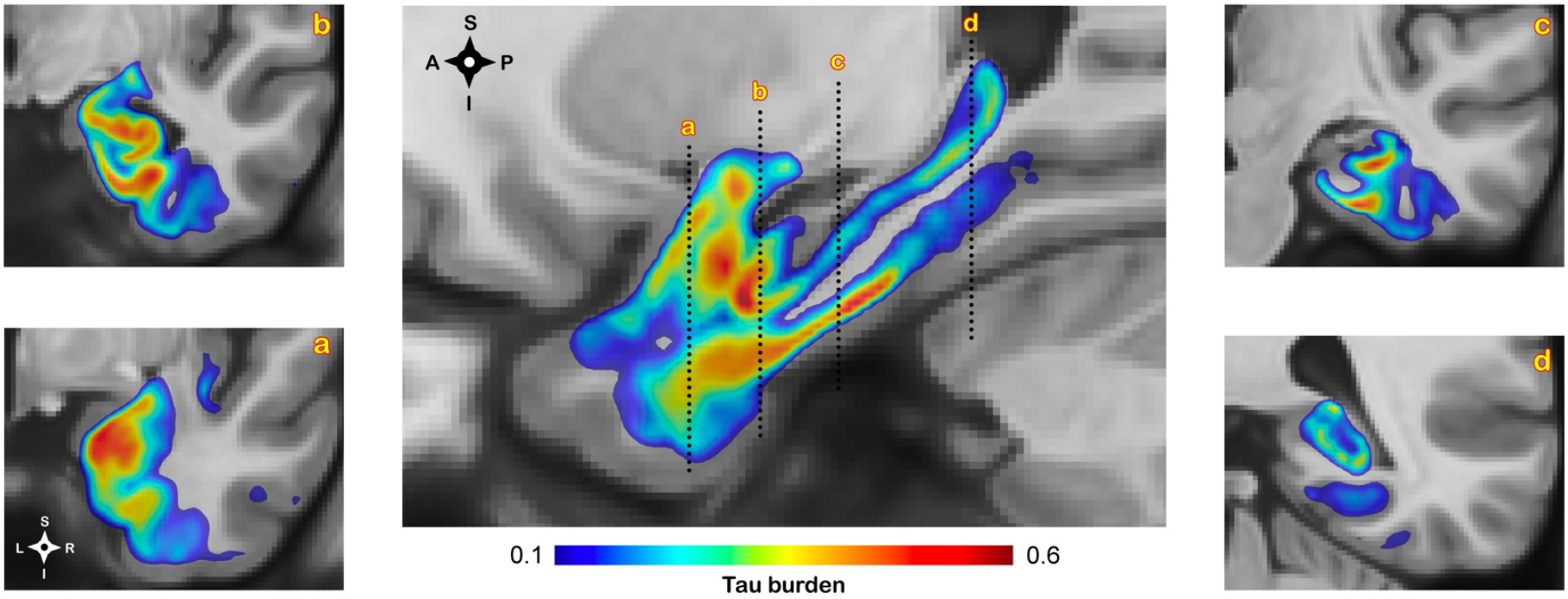

Suppl. Figure 1. Coronal and sagittal planes depict the overall Medial Temporal Lobe (MTL) neurofibrillary tangle burden, derived from a serial histological examination of 15 MTL specimens (for detailed methodology see, Yushkevich et al., 2021). These tau maps were used to create tau-based ROIs for MTL-AT and MTL-PM connectivity analyses.

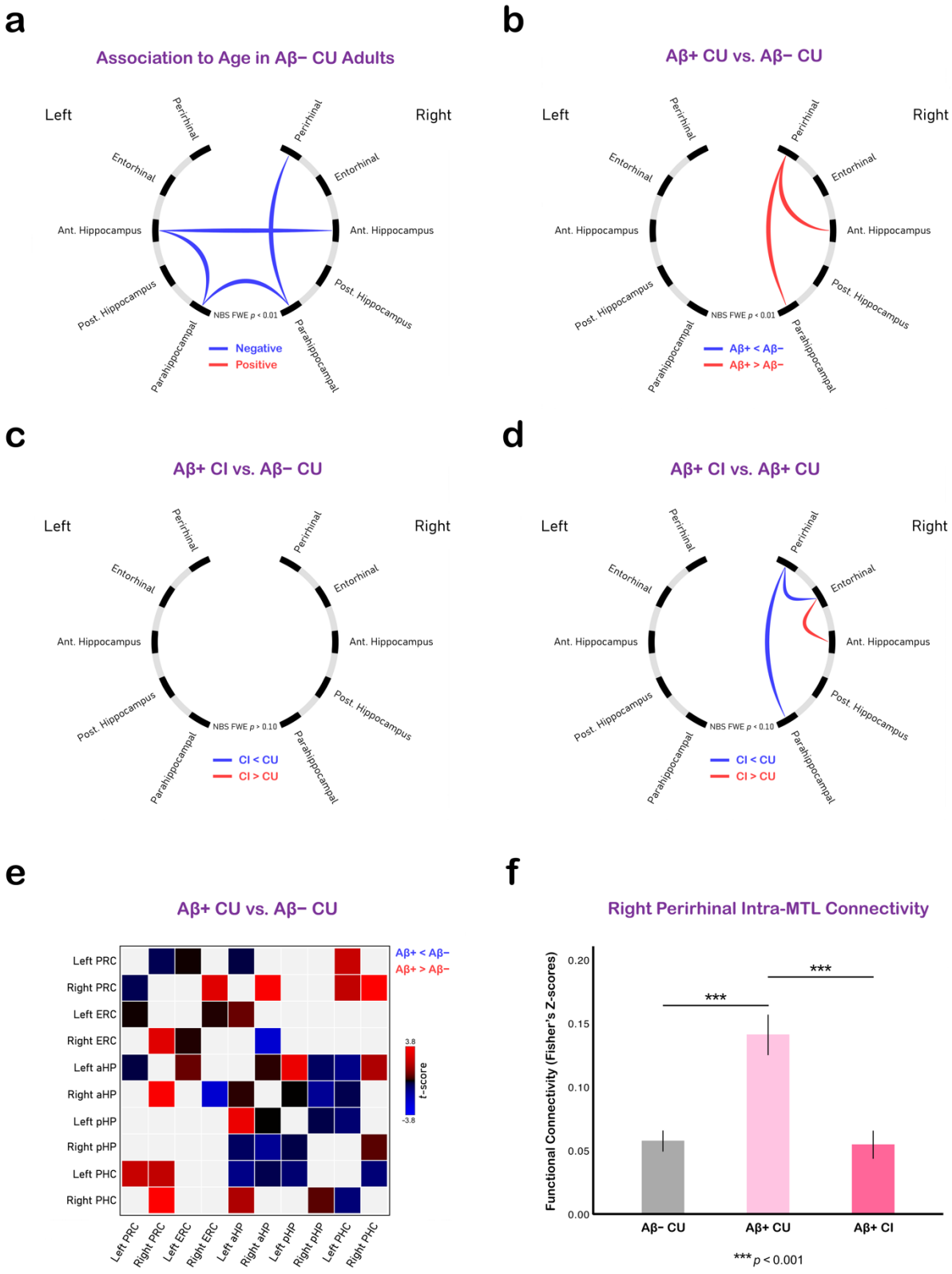

Suppl. Figure 2. This figure is a companion to Fig. 3 from the main text. Instead of canonical Pearson correlations, intra-MTL functional interactions were quantified using partial correlation coefficients, controlling for time courses from all other ASHS-T1 ROIs. Only those connections that represented *direct* intra-MTL functional interactions (see Fig. 2b in the main text) were analyzed. Connectograms depict the effects of **(a)** age and **(b-d)** AD progression on *direct* intra-MTL functional connectivity. **(e)** Matrix-form representation of *direct* intra-MTL connectivity differences between Aβ-positive individuals with preclinical AD and Aβ-negative age-matched controls. **(f)** Average strength of *direct* connections from the right PRC to other ASHS-T1 ROIs, in Aβ-negative normal agers, Aβ-positive cognitively normal individuals with preclinical AD, and Aβ-positive individuals with symptomatic disease. Abbreviations: PRC = Perirhinal Cortex; ERC = Entorhinal Cortex; PHC = Parahippocampal Cortex; aHP = Anterior Hippocampus; pHP = Posterior Hippocampus; CU = cognitively unimpaired; CI, cognitively impaired.

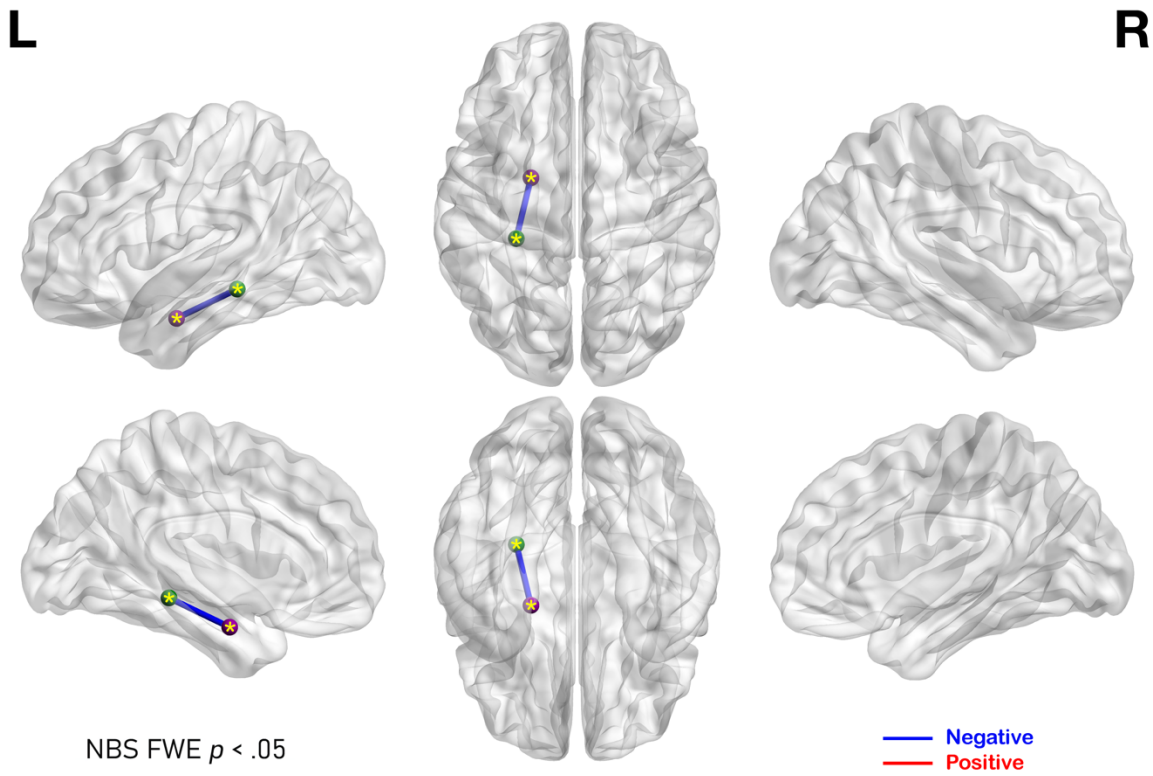

Suppl. Figure 3. The effect of normal aging on inter-module AT-PM connectivity. A single connection, linking the anterior and posterior tau-based MTL ROIs in the left hemisphere with each other, showed connectivity decline in amyloid-negative cognitively unimpaired agers.

SUPPLEMENTARY TABLES

Suppl. Table 1. MTL voxelwise temporal Signal-to-Noise Ratio (tSNR) for raw and preprocessed fMRI datasets, separated by group.

	PRC		ERC		PHC		Anterior HC		Posterior HC		Anterior Tau		Posterior Tau	
	Left	Right	Left	Right	Left	Right	Left	Right	Left	Right	Left	Right	Left	Right
Raw fMRI Data														
Young and Middle-Aged	13.63 (2.62)	13.44 (2.34)	9.55 (2.20)	10.15 (2.16)	21.90 (2.57)	21.62 (2.31)	16.97 (3.27)	18.10 (3.18)	21.74 (2.33)	21.82 (2.20)	14.27 (2.03)	15.49 (2.06)	20.83 (2.74)	20.60 (2.50)
Aβ- CU	12.48 (2.49)	11.91 (2.42)	8.92 (2.08)	9.29 (2.57)	19.45 (3.13)	18.86 (3.09)	16.14 (2.65)	16.81 (2.77)	20.61 (2.22)	20.35 (2.34)	13.55 (2.09)	14.41 (2.28)	19.52 (2.55)	19.12 (2.60)
Aβ+ CU	12.70 (2.08)	12.29 (2.34)	7.92 (1.86)	8.94 (2.44)	19.78 (2.38)	19.73 (2.52)	15.69 (3.48)	16.73 (3.61)	20.77 (2.19)	20.90 (2.18)	13.14 (1.91)	14.08 (2.51)	19.83 (2.25)	19.70 (2.01)
Aβ+ CI	12.00 (2.10)	11.56 (2.03)	7.95 (1.54)	8.90 (2.21)	19.13 (2.08)	18.61 (2.07)	15.33 (2.57)	15.99 (3.12)	20.47 (1.90)	20.36 (1.96)	13.63 (1.69)	14.43 (2.07)	19.44 (2.10)	19.33 (2.04)
Preprocessed fMRI Data														
Young and Middle-Aged	263.3 (51.5)	260.5 (51.3)	194.9 (40.1)	202.4 (34.5)	351.4 (47.3)	344.0 (45.7)	303.5 (58.6)	317.4 (55.2)	368.6 (41.4)	373.2 (39.8)	262.9 (46.8)	280.2 (44.9)	364.2 (51.0)	364.5 (44.1)
Aβ- CU	247.1 (47.3)	236.6 (48.9)	192.5 (32.4)	198.7 (35.8)	326.7 (38.9)	319.6 (46.8)	300.0 (42.2)	309.0 (42.6)	362.2 (39.2)	357.2 (38.8)	257.4 (38.0)	268.8 (38.9)	354.2 (45.5)	347.3 (47.0)
Aβ+ CU	244.8 (44.3)	240.0 (51.4)	176.9 (33.0)	190.5 (39.6)	322.1 (33.4)	321.5 (30.8)	296.8 (48.1)	309.7 (53.2)	362.3 (40.6)	365.5 (32.7)	253.4 (39.6)	264.8 (49.2)	354.8 (40.4)	352.7 (34.6)
Aβ+ CI	243.0 (43.4)	232.8 (42.4)	193.8 (28.1)	198.4 (40.0)	337.2 (42.4)	326.9 (35.4)	317.7 (47.7)	320.9 (52.3)	381.2 (46.9)	384.7 (40.7)	272.9 (38.0)	280.2 (41.9)	374.8 (51.7)	373.3 (46.6)

Suppl. Table 2. Displacement (FD) for raw and filtered realignment parameters, separated by group.

	Young and Middle-Aged (mm)	Aβ- CU (mm)	Aβ+ CU (mm)	Aβ+ CI (mm)
Raw Mean FD (SD)	0.1588 (0.0700)	0.2627 (0.1236)	0.2303 (0.0814)	0.2158 (0.0974)
Raw Max FD (SD)	0.6209 (0.5888)	1.1046 (1.0069)	1.0697 (0.7293)	1.2868 (1.0637)
Filtered Mean FD (SD)	0.0213 (0.0118)	0.0403 (0.0193)	0.0420 (0.0173)	0.0401 (0.0263)
Filtered Max FD (SD)	0.1698 (0.1354)	0.2273 (0.1900)	0.2633 (0.1737)	0.2915 (0.2155)

SUPPLEMENTARY REFERENCES

Asman, A. J., & Landman, B. A. (2013). Non-local statistical label fusion for multi-atlas segmentation. *Medical Image Analysis*, *17*(2), 194-208. https://doi.org/https://doi.org/10.1016/j.media.2012.10.002

Avants, B., & Gee, J. C. (2004). Geodesic estimation for large deformation anatomical shape averaging and interpolation. *Neuroimage*, *23 Suppl 1*, S139-150. https://doi.org/10.1016/j.neuroimage.2004.07.010

Avants, B. B., Epstein, C. L., Grossman, M., & Gee, J. C. (2008). Symmetric diffeomorphic image registration with cross-correlation: evaluating automated labeling of elderly and neurodegenerative brain. *Med Image Anal*, *12*(1), 26-41. https://doi.org/10.1016/j.media.2007.06.004

Benjamini, Y., & Hochberg, Y. (1995). Controlling the False Discovery Rate: A Practical and Powerful Approach to Multiple Testing. *Journal of the Royal Statistical Society. Series B (Methodological)*, *57*(1), 289-300. http://www.jstor.org.proxy.library.upenn.edu/stable/2346101

Dale, A. M., Fischl, B., & Sereno, M. I. (1999). Cortical surface-based analysis. I. Segmentation and surface reconstruction. *Neuroimage*, *9*(2), 179-194. https://doi.org/10.1006/nimg.1998.0395

Gorgolewski, K., Burns, C. D., Madison, C., Clark, D., Halchenko, Y. O., Waskom, M. L., & Ghosh, S. S. (2011). Nipype: a flexible, lightweight and extensible neuroimaging data processing framework in python. *Front Neuroinform*, *5*, 13. https://doi.org/10.3389/fninf.2011.00013

Jenkinson, M., Bannister, P., Brady, M., & Smith, S. (2002). Improved optimization for the robust and accurate linear registration and motion correction of brain images. *Neuroimage*, *17*(2), 825-841. https://doi.org/10.1016/s1053-8119(02)91132-8

Landau, S. M., Breault, C., Joshi, A. D., Pontecorvo, M., Mathis, C. A., Jagust, W. J., Mintun, M. A., & Alzheimer's Disease Neuroimaging, I. (2013). Amyloid-beta imaging with Pittsburgh compound B and florbetapir: comparing radiotracers and quantification methods. *J Nucl Med*, *54*(1), 70-77. https://doi.org/10.2967/jnumed.112.109009

Schaefer, A., Kong, R., Gordon, E. M., Laumann, T. O., Zuo, X. N., Holmes, A. J., Eickhoff, S. B., & Yeo, B. T. T. (2018). Local-Global Parcellation of the Human Cerebral Cortex from Intrinsic Functional Connectivity MRI. *Cereb Cortex*, *28*(9), 3095-3114. https://doi.org/10.1093/cercor/bhx179

Smith, S. M., Jenkinson, M., Woolrich, M. W., Beckmann, C. F., Behrens, T. E., Johansen-Berg, H., Bannister, P. R., De Luca, M., Drobnjak, I., Flitney, D. E., Niazy, R. K., Saunders, J., Vickers, J., Zhang, Y., De Stefano, N., Brady, J. M., & Matthews, P. M. (2004). Advances in functional and structural MR image analysis and implementation as FSL. *Neuroimage*, *23 Suppl 1*, S208-219. https://doi.org/10.1016/j.neuroimage.2004.07.051

Smith, S. M., & Nichols, T. E. (2009). Threshold-free cluster enhancement: addressing problems of smoothing, threshold dependence and localisation in cluster inference. *Neuroimage*, *44*(1), 83-98. https://doi.org/10.1016/j.neuroimage.2008.03.061

Tustison, N. J., Avants, B. B., Cook, P. A., Zheng, Y., Egan, A., Yushkevich, P. A., & Gee, J. C. (2010). N4ITK: improved N3 bias correction. *IEEE Trans Med Imaging*, *29*(6), 1310-1320. https://doi.org/10.1109/TMI.2010.2046908

Wang, H., Suh, J. W., Das, S. R., Pluta, J. B., Craige, C., & Yushkevich, P. A. (2013). Multi-Atlas Segmentation with Joint Label Fusion. *IEEE Trans Pattern Anal Mach Intell*, *35*(3), 611-623. https://doi.org/10.1109/TPAMI.2012.143

Whitfield-Gabrieli, S., & Nieto-Castanon, A. (2012). Conn: a functional connectivity toolbox for correlated and anticorrelated brain networks. *Brain Connect*, *2*(3), 125-141. https://doi.org/10.1089/brain.2012.0073

Zhang, Y., Brady, M., & Smith, S. (2001). Segmentation of brain MR images through a hidden Markov random field model and the expectation-maximization algorithm. *IEEE Trans Med Imaging*, *20*(1), 45-57. https://doi.org/10.1109/42.906424